

PREPARED FOR SUBMISSION TO JCAP

Mass calibration of DES Year-3 clusters via SPT-3G CMB cluster lensing

SPT-3G & DES Collaborations

B. Ansarinejad,¹ S. Raghunathan,² T. M. C. Abbott,³ P. A. R. Ade,⁴
M. Aguena,⁵ O. Alves,⁶ A. J. Anderson,^{8,9,7} F. Andrade-Oliveira,⁶
M. Archipley,^{10,2} L. Balkenhol,¹¹ K. Benabed,¹¹ A. N. Bender,^{12,8,9}
B. A. Benson,^{7,8,9} E. Bertin,^{11,40} F. Bianchini,^{13,14,15} L. E. Bleem,^{12,8}
S. Bocquet,³⁸ F. R. Bouchet,¹¹ D. Brooks,⁴¹ L. Bryant,¹⁶
D. L. Burke,^{13,15} E. Camphuis,¹¹ J. E. Carlstrom,^{8,16,17,12,9}
A. Carnero Rosell,^{42,5} J. Carretero,^{42,5} F. J. Castander,⁴⁴ T. W. Cecil,¹²
C. L. Chang,^{12,8,9} P. Chaubal,¹ P. M. Chichura,^{17,8} T.-L. Chou,^{17,8}
A. Coerver,¹⁸ M. Costanzi,^{46,47,48} T. M. Crawford,^{8,9}
A. Cukierman,^{13,15,14} L. N. da Costa,⁵ C. Daley,¹⁰ T. M. Davis,⁵⁰
T. de Haan,¹⁹ S. Desai,⁵² J. De Vicente,⁵¹ K. R. Dibert,^{9,8}
M. A. Dobbs,^{20,21} P. Doel,⁴¹ A. Doussot,¹¹ C. Doux,^{53,54} D. Dutcher,²²
W. Everett,²³ C. Feng,²⁴ K. R. Ferguson,²⁵ I. Ferrero,⁵⁵ K. Fichman,^{17,8}
A. Foster,²⁶ J. Frieman,^{7,8} S. Galli,¹¹ A. E. Gambrel,⁸
J. García-Bellido,⁵⁶ R. W. Gardner,¹⁶ E. Gaztanaga,^{45,46} F. Ge,²⁷
G. Giannini,^{44,8} N. Goeckner-Wald,^{14,13} S. Grandis,³⁹
R. A. Gruendl,^{2,10} R. Gualtieri,¹² F. Guidi,¹¹ S. Guns,¹⁸ G. Gutierrez,⁷
N. W. Halverson,^{28,29} S. R. Hinton,⁵⁰ E. Hivon,¹¹ G. P. Holder,²⁴
D. L. Hollowood,⁵⁷ W. L. Holzzapfel,¹⁸ K. Honscheid,^{58,59} J. C. Hood,⁸
N. Huang,¹⁸ D. J. James,³⁶ F. Kéruzoré,¹² L. Knox,²⁷ M. Korman,²⁶
C.-L. Kuo,^{13,14,15} A. T. Lee,^{18,30} S. Lee,⁶⁰ K. Levy,¹ A. E. Lowitz,⁸
C. Lu,²⁴ A. Maniyar,^{13,14,15} J. L. Marshall,⁶¹ J. Mena-Fernández,⁶²
F. Menanteau,^{10,2} R. Miquel,^{63,44} M. Millea,¹⁸ J. J. Mohr,^{64,38}
J. Montgomery,²⁰ Y. Nakato,¹⁴ T. Natoli,⁸ G. I. Noble,^{31,32}
V. Novosad,³³ R. L. C. Ogando,⁶⁵ Y. Omori,^{9,8} S. Padin,^{8,34}
A. Palmese,⁶⁶ Z. Pan,^{12,8,17} P. Paschos,¹⁶ M. E. S. Pereira,⁴⁹
A. Pieres,^{5,65} A. A. Plazas Malagón,^{13,15} K. Prabhu,²⁷ W. Quan,^{17,8}
A. Rahlin,^{7,8} M. Rahimi,¹ C. L. Reichardt,¹ K. Reil,¹⁵ A. K. Romer,⁶⁶

**M. Rouble,²⁰ J. E. Ruhl,²⁶ E. Sanchez,⁵¹ D. Sanchez Cid,⁵¹
E. Schiappucci,¹ I. Sevilla-Noarbe,⁵¹ G. Smecher,³⁵ M. Smith,⁶⁸
J. A. Sobrin,^{7,8} A. A. Stark,³⁶ J. Stephen,¹⁶ E. Suchyta,⁶⁹ A. Suzuki,³⁰
M. E. C. Swanson,² C. Tandoi,¹⁰ G. Tarle,⁶ K. L. Thompson,^{13,14,15}
B. Thorne,²⁷ C. Trendafilova,² C. Tucker,⁴ C. Umilta,²⁴
J. D. Vieira,^{10,24,2} G. Wang,¹² N. Weaverdyck,^{6,30} N. Whitehorn,³⁷
P. Wiseman,⁶⁸ W. L. K. Wu,^{13,15} V. Yefremenko,¹² M. R. Young,^{7,8}
J. A. Zebrowski.^{8,9,7}**

¹School of Physics, University of Melbourne, Parkville, VIC 3010, Australia

²Center for Astrophysical Surveys, National Center for Supercomputing Applications, Urbana, IL, 61801, USA

³Cerro Tololo Inter-American Observatory, NSF's NOIRLab, Casilla 603, La Serena, Chile

⁴School of Physics and Astronomy, Cardiff University, Cardiff CF24 3YB, United Kingdom

⁵Laboratório Interinstitucional de e-Astronomia - LIneA, Rua Gal. José Cristino 77, Rio de Janeiro, RJ - 20921-400, Brazil

⁶Department of Physics, University of Michigan, Ann Arbor, MI 48109, USA

⁷Fermi National Accelerator Laboratory, P.O. Box 500, Batavia, IL, 60510, USA

⁸Kavli Institute for Cosmological Physics, University of Chicago, 5640 South Ellis Avenue, Chicago, IL, 60637, USA

⁹Department of Astronomy and Astrophysics, University of Chicago, 5640 South Ellis Avenue, Chicago, IL, 60637, USA

¹⁰Department of Astronomy, University of Illinois Urbana-Champaign, 1002 West Green Street, Urbana, IL, 61801, USA

¹¹Sorbonne Université, CNRS, UMR 7095, Institut d'Astrophysique de Paris, 98 bis bd Arago, 75014 Paris, France

¹²High-Energy Physics Division, Argonne National Laboratory, 9700 South Cass Avenue., Lemont, IL, 60439, USA

¹³Kavli Institute for Particle Astrophysics and Cosmology, Stanford University, 452 Lomita Mall, Stanford, CA, 94305, USA

¹⁴Department of Physics, Stanford University, 382 Via Pueblo Mall, Stanford, CA, 94305, USA

¹⁵SLAC National Accelerator Laboratory, 2575 Sand Hill Road, Menlo Park, CA, 94025, USA

¹⁶Enrico Fermi Institute, University of Chicago, 5640 South Ellis Avenue, Chicago, IL, 60637, USA

¹⁷Department of Physics, University of Chicago, 5640 South Ellis Avenue, Chicago, IL, 60637, USA

¹⁸Department of Physics, University of California, Berkeley, CA, 94720, USA

¹⁹High Energy Accelerator Research Organization (KEK), Tsukuba, Ibaraki 305-0801, Japan

²⁰Department of Physics and McGill Space Institute, McGill University, 3600 Rue University, Montreal, Quebec H3A 2T8, Canada

²¹Canadian Institute for Advanced Research, CIFAR Program in Gravity and the Extreme Universe, Toronto, ON, M5G 1Z8, Canada

²²Joseph Henry Laboratories of Physics, Jadwin Hall, Princeton University, Princeton, NJ 08544, USA

²³Department of Astrophysical and Planetary Sciences, University of Colorado, Boulder, CO, 80309, USA

- ²⁴Department of Physics, University of Illinois Urbana-Champaign, 1110 West Green Street, Urbana, IL, 61801, USA
- ²⁵Department of Physics and Astronomy, University of California, Los Angeles, CA, 90095, USA
- ²⁶Department of Physics, Case Western Reserve University, Cleveland, OH, 44106, USA
- ²⁷Department of Physics & Astronomy, University of California, One Shields Avenue, Davis, CA 95616, USA
- ²⁸CASA, Department of Astrophysical and Planetary Sciences, University of Colorado, Boulder, CO, 80309, USA
- ²⁹Department of Physics, University of Colorado, Boulder, CO, 80309, USA
- ³⁰Physics Division, Lawrence Berkeley National Laboratory, Berkeley, CA, 94720, USA
- ³¹Dunlap Institute for Astronomy & Astrophysics, University of Toronto, 50 St. George Street, Toronto, ON, M5S 3H4, Canada
- ³²David A. Dunlap Department of Astronomy & Astrophysics, University of Toronto, 50 St. George Street, Toronto, ON, M5S 3H4, Canada
- ³³Materials Sciences Division, Argonne National Laboratory, 9700 South Cass Avenue, Lemont, IL, 60439, USA
- ³⁴California Institute of Technology, 1200 East California Boulevard., Pasadena, CA, 91125, USA
- ³⁵Three-Speed Logic, Inc., Victoria, B.C., V8S 3Z5, Canada
- ³⁶Harvard-Smithsonian Center for Astrophysics, 60 Garden Street, Cambridge, MA, 02138, USA
- ³⁷Department of Physics and Astronomy, Michigan State University, East Lansing, MI 48824, USA
- ³⁸University Observatory, Faculty of Physics, Ludwig-Maximilians-Universität, Scheinerstr. 1, 81679 Munich, Germany
- ³⁹Universität Innsbruck, Institut für Astro- und Teilchenphysik, Technikerstr. 25/8, 6020 Innsbruck, Austria
- ⁴⁰Sorbonne Universités, UPMC Univ Paris 06, UMR 7095, Institut d'Astrophysique de Paris, F-75014, Paris, France
- ⁴¹Department of Physics & Astronomy, University College London, Gower Street, London, WC1E 6BT, UK
- ⁴²Instituto de Astrofísica de Canarias, E-38205 La Laguna, Tenerife, Spain
- ⁴³Universidad de La Laguna, Dpto. Astrofísica, E-38206 La Laguna, Tenerife, Spain
- ⁴⁴Institut de Física d'Altes Energies (IFAE), The Barcelona Institute of Science and Technology, Campus UAB, 08193 Bellaterra (Barcelona) Spain
- ⁴⁵Institut d'Estudis Espacials de Catalunya (IEEC), 08034 Barcelona, Spain
- ⁴⁶Institute of Space Sciences (ICE, CSIC), Campus UAB, Carrer de Can Magrans, s/n, 08193 Barcelona, Spain
- ⁴⁶Astronomy Unit, Department of Physics, University of Trieste, via Tiepolo 11, I-34131 Trieste, Italy
- ⁴⁷INAF-Osservatorio Astronomico di Trieste, via G. B. Tiepolo 11, I-34143 Trieste, Italy
- ⁴⁸Institute for Fundamental Physics of the Universe, Via Beirut 2, 34014 Trieste, Italy
- ⁴⁹Hamburger Sternwarte, Universität Hamburg, Gojenbergsweg 112, 21029 Hamburg, Germany
- ⁵⁰School of Mathematics and Physics, University of Queensland, Brisbane, QLD 4072, Australia
- ⁵¹Centro de Investigaciones Energéticas, Medioambientales y Tecnológicas (CIEMAT), Madrid, Spain
- ⁵²Department of Physics, IIT Hyderabad, Kandi, Telangana 502285, India
- ⁵³Department of Physics and Astronomy, University of Pennsylvania, Philadelphia, PA 19104, USA
- ⁵⁴Université Grenoble Alpes, CNRS, LPSC-IN2P3, 38000 Grenoble, France

- ⁵⁵Institute of Theoretical Astrophysics, University of Oslo. P.O. Box 1029 Blindern, NO-0315 Oslo, Norway
- ⁵⁶Instituto de Fisica Teorica UAM/CSIC, Universidad Autonoma de Madrid, 28049 Madrid, Spain
- ⁵⁷Santa Cruz Institute for Particle Physics, Santa Cruz, CA 95064, USA
- ⁵⁸Center for Cosmology and Astro-Particle Physics, The Ohio State University, Columbus, OH 43210, USA
- ⁵⁹Department of Physics, The Ohio State University, Columbus, OH 43210, USA
- ⁶⁰Jet Propulsion Laboratory, California Institute of Technology, 4800 Oak Grove Dr., Pasadena, CA 91109, USA
- ⁶¹George P. and Cynthia Woods Mitchell Institute for Fundamental Physics and Astronomy, and Department of Physics and Astronomy, Texas A&M University, College Station, TX 77843, USA
- ⁶²LPSC Grenoble - 53, Avenue des Martyrs 38026 Grenoble, France
- ⁶³Institució Catalana de Recerca i Estudis Avançats, E-08010 Barcelona, Spain
- ⁶⁴Max Planck Institute for Extraterrestrial Physics, Giessenbachstrasse, 85748 Garching, Germany
- ⁶⁵Observatório Nacional, Rua Gal. José Cristino 77, Rio de Janeiro, RJ - 20921-400, Brazil
- ⁶⁶Department of Physics, Carnegie Mellon University, Pittsburgh, Pennsylvania 15312, USA
- ⁶⁷Department of Physics and Astronomy, Pevensey Building, University of Sussex, Brighton, BN1 9QH, UK
- ⁶⁸School of Physics and Astronomy, University of Southampton, Southampton, SO17 1BJ, UK
- ⁶⁹Computer Science and Mathematics Division, Oak Ridge National Laboratory, Oak Ridge, TN 37831

E-mail: Behzad.ansarinejad@unimelb.edu.au, srinirag@illinois.edu

Abstract. We measure the stacked lensing signal in the direction of galaxy clusters in the Dark Energy Survey Year 3 (DES Y3) redMaPPer sample, using cosmic microwave background (CMB) temperature data from SPT-3G, the third-generation CMB camera on the South Pole Telescope (SPT). Here, we estimate the lensing signal using temperature maps constructed from the initial 2 years of data from the SPT-3G ‘Main’ survey, covering 1500 deg² of the Southern sky. We then use this lensing signal as a proxy for the mean cluster mass of the DES sample. The thermal Sunyaev–Zel’dovich (tSZ) signal, which can contaminate the lensing signal if not addressed, is isolated and removed from the data before obtaining the mass measurement. In this work, we employ three versions of the redMaPPer catalogue: a Flux-Limited sample containing 8865 clusters, a Volume-Limited sample with 5391 clusters, and a Volume&Redshift-Limited sample with 4450 clusters. For the three samples, we detect the CMB lensing signal at a significance of 10.3σ , 10.0σ , and 9.6σ and find the mean cluster masses to be $M_{200m} = 1.66 \pm 0.13$ [stat.] ± 0.03 [sys.], 1.97 ± 0.18 [stat.] ± 0.05 [sys.], and 2.11 ± 0.20 [stat.] ± 0.05 [sys.] $\times 10^{14} M_{\odot}$, respectively. This is a factor of ~ 2 improvement relative to the precision of measurements with previous generations of SPT surveys and the most constraining cluster mass measurements using CMB cluster lensing to date. Overall, we find no significant tensions between our results and masses given by redMaPPer mass–richness scaling relations of previous works, which were calibrated using CMB cluster lensing, optical weak lensing, and velocity dispersion measurements from various combinations of DES, SDSS and Planck data. We then divide our sample into 3 redshift and 3 richness bins, finding no significant discrepancies with optical weak-lensing calibrated masses in these bins. We forecast a 5.8% constraint on the mean cluster mass of the DES Y3 sample with the complete SPT-3G surveys when using both temperature and polarization data and including an additional ~ 1400 deg² of observations from the ‘Extended’ SPT-3G survey.

Keywords: galaxy clusters, gravitational lensing, weak gravitational lensing

Contents

1	Introduction	1
2	Datasets	4
2.1	SPT-3G CMB data	4
2.2	tSZ-nulled SPT-3G map	4
2.3	DES Y3 redMaPPer galaxy clusters	4
3	Pipeline description and validation	6
3.1	Lensing estimator	6
3.2	Lensing dipole models	7
3.3	Stacked cluster mass likelihood	7
3.4	Simulations & pipeline validation	8
4	Results and Discussion	9
4.1	Pipeline verification results	9
4.2	Mean cluster mass	9
4.3	Systematics	10
4.3.1	Cluster tSZ Signal and Residual Foregrounds	10
4.3.2	Cluster miscentering	11
4.3.3	Filtering model	12
4.3.4	Beam uncertainties	12
4.3.5	Optical weak lensing systematics	12
4.4	Cluster mass–richness scaling relation	13
4.5	Mean cluster mass as a function of redshift	13
4.6	Forecasts	14
5	Conclusions	15

1 Introduction

Galaxy clusters are the most massive gravitationally collapsed objects and are the culmination of structure growth processes across cosmic time. As a result, cluster number counts as a function of cluster mass and redshift provide a sensitive probe of cosmological parameters that influence the growth of structure and the geometry of the Universe [see reviews by 1, 2]. These parameters include the matter density parameter, Ω_m ; the normalisation of the matter power spectrum on the scale of $8 h^{-1}\text{Mpc}$, σ_8 ; the dark energy equation of state parameter, w ; as well as the sum of neutrino masses, $\sum m_\nu$ [see e.g. 3–6]. These constraints are highly complementary to those derived from analyses of baryon acoustic oscillations (BAO; [7, 8]), cosmic microwave background (CMB; [9–11]), as well as auto- and cross-correlation analyses of optical weak gravitational lensing and galaxy clustering (3x2pt; [12–14]) as these measurements have different parameter degeneracies and independent sources of systematics.

However, cosmological analysis of galaxy cluster samples is currently limited by our ability to reconstruct the mass distribution of the cluster sample (a problem called *mass calibration*; see e.g. Section VI of [15] and Section 4 of [5], for a discussion of the impact of systematics on recent cluster

cosmology analyses). In the near future, surveys such as eROSITA [16], LSST [17], Euclid [18] and CMB-S4 [19] will increase the cluster sample size compared to existing surveys by an order of magnitude, significantly reducing limitations due to statistical uncertainties. In preparation for these datasets, it is, therefore, crucial to improve our understanding of sources of systematic uncertainty that could impact commonly used cluster detection and mass calibration methods. In the optical regime, weak gravitational lensing is the most common cluster mass measurement approach [see 20, for a review]. Weak lensing offers the advantage of probing the total cluster mass with weak dependence on complex baryonic physics, which could affect the mass-observable scaling relations of the thermal Sunyaev–Zel’dovich (tSZ) decrement, X-ray luminosity, and cluster richness. Weak lensing is, however, impacted by various sources of systematics error including bias in photometric redshift estimates, galaxy shape modelling errors and contamination of the lensed galaxy sample with cluster member or foreground galaxies [21–23]. Calibration of these effects has led to a systematic floor smaller than 2% on the halo mass [24, 25] if source galaxies can be reliably selected in the background of the cluster sample.

CMB cluster lensing is a promising alternative technique for measuring the masses of galaxy clusters. In this phenomenon, CMB photons passing through galaxy clusters’ gravitational potential wells are deflected and due to the small-scale CMB gradient, form arcminute scale dipoles with amplitudes of $\lesssim 10\mu\text{K}$ [26, 27]. Measurements of these dipoles can, therefore, be used as a proxy for the cluster mass. Furthermore, CMB cluster lensing and optical weak lensing have mostly independent systematics (though projection effects will impact both observables; see Section 4.2.5 for details), enabling us to verify whether these systematics have been correctly characterised and accounted for. Additionally, since the source plane of CMB lensing is the surface of last scattering at $z \sim 1100$, mass calibration can also be carried out for higher cluster redshifts, where optical lensing starts to suffer from unreliable background source selection. This makes CMB cluster lensing an essential tool for cluster mass measurements in upcoming datasets such as CMB-S4, which greatly increase the size of high redshift cluster samples by detecting thousands of clusters at $z > 1$ [28].

Over the past two decades, several different methods have been developed to measure the CMB cluster and galaxy lensing signal from CMB temperature and polarization maps [27, 29–36]. In recent years, a number of studies have obtained the first significant detections of CMB cluster lensing using data from various CMB experiments. Using CMB temperature data from the SPT-SZ survey conducted with the South Pole Telescope (SPT) and a sample of 513 clusters [37] detected with the same data, [38] obtained a 3.1σ measurement of the CMB cluster lensing signal. Using data from the Atacama Cosmology Telescope (ACT) and various galaxy samples, [39] and [40] obtained a 3.2σ and 4.2σ detection of the signal, respectively. Similar studies using the Planck CMB data include [5] and [41], where the lensing signal was measured at $\sim 5\sigma$ for SZ-detected galaxy cluster samples, and [42], where a sample of 12.4 million galaxies selected from the WISE and SCOS surveys were used as tracers of dark matter halos, obtaining a 17σ measurement of the lensing signal.

Past studies have also applied CMB cluster lensing to calibrate the scaling relation between cluster mass and richness for different cluster samples detected with the redMaPPer algorithm [43]. [44] obtained a 10% constraint on the richness–mass scaling relation using the Planck CMB data and optically detected clusters in the Sloan Digital Sky Survey (SDSS) data presented by [43]. Later, [45] used the SPT-SZ CMB temperature map to obtain a 17% constraint on the amplitude of the mass–richness scaling relation of redMaPPer clusters detected in the Dark Energy Survey [DES 46] Year 1 data [47], while [48] obtained a $\sim 20\%$ measurement of the same scaling relation for the DES Year 3 (Y3) redMaPPer cluster sample, using CMB temperature maps from the SPTpol survey [49]. [35] also used the same datasets to obtain the first detection of the CMB cluster lensing signal using only the polarization data, obtaining a $\sim 28\%$ mass constraint for richness $\lambda > 10$ clusters in the DES

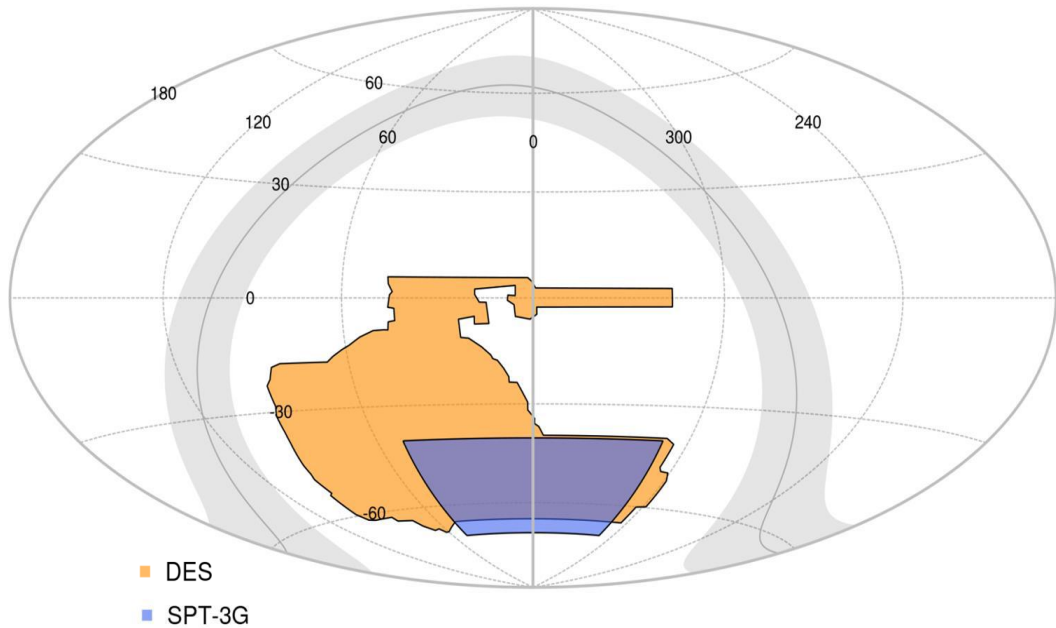


Figure 1. The $\sim 1400 \text{ deg}^2$ overlap between the $\sim 1500 \text{ deg}^2$ SPT-3G Main field (blue) and the $\sim 5000 \text{ deg}^2$ DES (orange) survey footprints. The grey band marks the galactic plane.

Y3 sample.

One of the main challenges in measuring the CMB cluster lensing signal is overcoming contamination due to various astrophysical foregrounds which could bias the cluster mass measurements if they are not accounted for. These sources of contamination include the tSZ and kinetic SZ (kSZ) effects, as well as the cosmic infrared background (CIB) due to the presence of dusty galaxies in the clusters (see [50] for a comprehensive discussion of the impact of these systematics on CMB cluster lensing measurements). Various techniques have been developed to overcome these sources of contamination, including cleaning the large-scale CMB gradient using a Quadratic Estimator (QE) to overcome the tSZ bias, as proposed by [51]. [52] later developed a modified QE that overcame tSZ, kSZ, and CIB contamination by inpainting the large-scale gradient in the CMB maps to remove the cluster emission. [35] presented a new estimator to measure the lensing dipole of stacked images, based on rotating cluster-centred CMB map cutouts along the direction of locally measured background CMB gradients. This approach is much simpler and less computationally expensive than the other alternative techniques and we adopt this method for measuring CMB cluster lensing in this study.

The layout of this paper is as follows. We present a summary of the galaxy cluster sample and the CMB maps used in our analysis in Section 2, followed by a description of our methods and pipeline verification with simulations in Section 3. We then present our results and compare them with various other DES cluster mass measurements from the literature in Section 4. We conclude by presenting a summary of our findings and their implications in Section 5. Throughout, we assume a Λ CDM cosmology with $h = 0.6774$, $\Omega_m = 0.307$, and $\Omega_\Lambda = 0.693$. In this work, we express cluster masses as M_{200m} , defined as the mass enclosed within a sphere whose average density is 200 times that of the mean matter density of the Universe, $\bar{\rho}_m$, at the cluster redshift.

2 Datasets

In this section, we provide a brief description of the datasets and sample selection used in our CMB cluster lensing analysis.

2.1 SPT-3G CMB data

SPT is a 10-meter telescope located at the Amundsen-Scott South Pole station [53], optimised for low-noise observations of the temperature and polarization of the CMB. SPT-3G [54] is the third and latest receiver installed on the telescope, with the SPT-3G Main field covering a $\sim 1500 \text{ deg}^2$ footprint defined by $310^\circ < \text{RA} < 50^\circ$ and $-70^\circ < \text{DEC} < -42^\circ$. After masking point sources in the CMB data (see Section 2.3) and taking into account the masked area in the DES cluster sample, we are left with an overlap of $\sim 1350 \text{ deg}^2$ (see Figure 1) between the SPT-3G survey and the DES cluster catalogue. In this work, we use data from the initial two years of the SPT-3G survey observation (2019-2020). While the analysis of this paper is only performed using temperature data, we note that the inclusion of the initial two years of SPT-3G polarization data is expected to reduce the mass uncertainty by $\sim 10\%$. We leave the polarization measurement to future works and provide forecasts for mass constraints using temperature and polarization data from the full survey depth, as well as data from the SPT-3G ‘Extended’ survey (which provides an additional $\sim 1400 \text{ deg}^2$ of overlap with DES albeit at a lower sensitivity) in Section 4.6. In addition to the Main and Extended SPT-3G surveys, an additional $\sim 6000 \text{ deg}^2$ of the Southern sky will be observed for one year in the SPT-3G ‘Wide’ survey. However, due to the relatively small additional overlap area with DES and the higher noise levels of these data, the Wide survey observations will not provide a significant improvement in the S/N of the CMB cluster lensing measurements, and we do not include these in our forecasts.

SPT-3G Main survey observations are conducted in the 95, 150, and 220 GHz bands with $1.6'$, $1.2'$, and $1.0'$ full width at half maximum beams and white noise levels of ~ 5 , 4, and $15 \mu\text{K}$ – arcmin for the first two years of observations, in the three bands respectively. For each SPT-3G detector, the raw data are composed of digitised time-ordered data (TOD) that are converted to CMB temperature units (for details of the SPT-3G map making and data processing, see [55]). During map making, we apply a $300 < \ell_x < 13000$ bandpass filter to the TOD. In this analysis, we use maps based on a minimum-variance combination of the 95, 150, and 220 GHz data, with Sanson-Flamsteed flat-sky projection [56] and $0.5'$ pixels.

2.2 tSZ-nulled SPT-3G map

As described in Section 3.1 our lensing estimator requires the estimation of the local CMB gradient at the location of each galaxy cluster. For this purpose, we use a tSZ-nulled CMB map constructed by performing an internal linear combination (ILC) of 95, 150, and 220 GHz data. As this map does not contain the tSZ signal, it allows for a more accurate estimation of the CMB gradient direction and amplitude, which in turn improves the S/N of our lensing dipole measurement.

2.3 DES Y3 redMaPPer galaxy clusters

DES has a $\sim 5000 \text{ deg}^2$ footprint with imaging taken in the g , r , i , z , and Y bands via the Dark Energy Camera [57] installed on the 4m Blanco telescope at the Cerro Tololo Observatory. The survey has completed the sixth and final year of observations, and here we use cluster samples detected using data from the first 3 years of the survey [58]. We refer the reader to [59] for a description of the application of the redMaPPer algorithm to the DES survey. In this work, we perform our analysis based on three redMaPPer cluster samples: a Flux-Limited sample, a Volume-Limited sample, and the Volume-Limited sample limited to the redshift range $0.2 < z < 0.65$. Henceforth, we shall refer

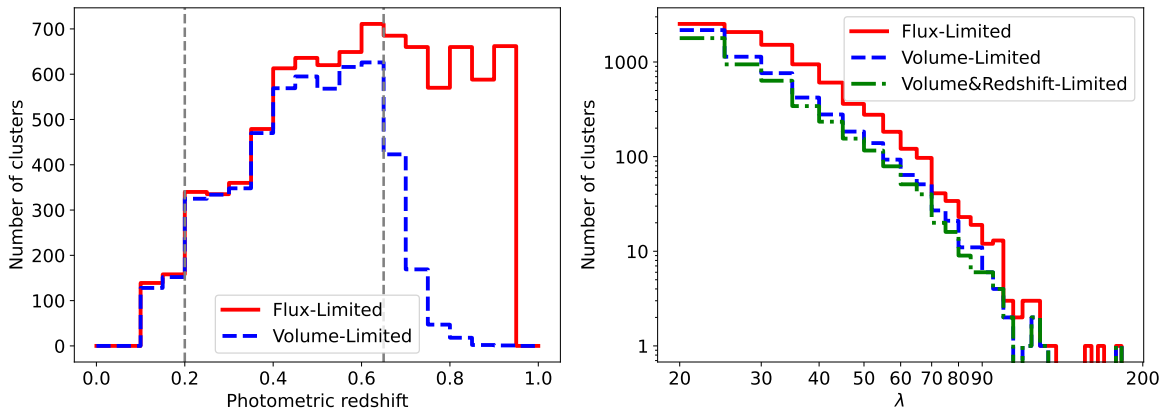


Figure 2. *Left panel:* The photometric redshift distribution of the DES Y3 flux and Volume-Limited redMaPPer cluster samples. The vertical dashed lines indicate the redshift cuts applied to the Volume-Limited sample. Here, we can see that most additional clusters in the Flux-Limited sample relative to the Volume-Limited sample are at $z > 0.6$. *Right panel:* The richness distribution of the Flux-, Volume- and Volume&Redshift-Limited samples. Although Volume-Limited samples contain fewer clusters, they follow a richness distribution similar to the Flux-Limited sample.

Table 1. The number of clusters in the 3 redshift and richness subsamples of our Volume&Redshift-Limited sample. The bins were chosen to have approximately equal numbers of clusters.

bin definition	clusters per bin
$0.20 < z < 0.40$	1477
$0.40 < z < 0.53$	1480
$0.53 < z < 0.65$	1493
$20 < \lambda < 24$	1491
$24 < \lambda < 32$	1530
$32 < \lambda$	1429

to the latter as the Volume&Redshift-Limited sample. While the Flux-Limited sample contains a significantly higher number of clusters at $z > 0.65$, which would yield a lensing measurement with a higher S/N, the Volume-Limited sample is limited to varying redshifts which are determined based on the magnitude limit of the observations across the survey footprint. The Volume&Redshift-Limited sample is then created to ensure sample uniformity across the survey footprint and match the selection applied to the sample used for the DES Y3 cluster cosmology analysis.

In all cases, samples are limited to clusters with richness $\lambda \geq 20$. Upon masking clusters within 1° of the edges of the SPT-3G footprint and within $10'$ of bright point sources (≥ 6 mJy at 150GHz), we are left with 4450, 5391, and 8865 clusters in the Volume&Redshift-Limited, Volume-Limited, and Flux-Limited samples, respectively. The photometric redshift and richness distributions of the three samples are shown in Figure 2. The median photometric redshifts of the Volume- and Flux-Limited samples are ~ 0.47 and ~ 0.61 , with median uncertainties of $\sigma_z/(1+z) = 0.006$ and 0.008 , respectively.

To investigate the potential redshift or richness dependence of the cluster mass–richness scaling relation, we divide the Volume&Redshift-Limited sample into 3 redshift and richness bins with an approximately equal number of clusters, as shown in Table 1.

3 Pipeline description and validation

3.1 Lensing estimator

We adopt the lensing estimator introduced by [35], which is briefly described here. Using the tSZ-nulled map described in Section 2.2, the algorithm first extracts $60' \times 60'$ cutouts, centred on the location of N_{clus} clusters and N_{rand} random locations. The code then determines the median gradient direction $\theta_{\nabla} = \tan^{-1}(\nabla_y/\nabla_x)$ from the central $6' \times 6'$ region of each cutout. The noise penalty in the gradient estimation is reduced by applying a Wiener filter given by:

$$W_{\ell} = \begin{cases} C_{\ell}(C_{\ell} + N_{\ell})^{-1}, & \ell \leq 2000 \\ 0, & \text{otherwise} \end{cases}, \quad (3.1)$$

to the $60' \times 60'$ cutouts, where C_{ℓ} and N_{ℓ} are the data and noise power spectra, with the latter calculated using half-difference maps.

Central $10' \times 10'$ cutouts, \mathbf{d} , are then extracted from the SPT-3G map and rotated along the direction of the gradients, allowing for the stacking of the lensing dipoles which are oriented along the direction of the local CMB gradient.¹ At this stage, a weight is assigned to each cluster given by $w = w_n w_g$, where the w_n component is based on the inverse noise variance σ^2 at the location of the cluster. The weight, w_g , is based on the median magnitude of the local gradient $\sqrt{\nabla_x^2 + \nabla_y^2}$, which serves to maximize the S/N of the measured dipole amplitude given its proportionality to the gradient amplitude.

The cutouts are then mean subtracted² and stacked to obtain the weighted stacks \mathbf{s}_c and \mathbf{s}_r at the location of clusters and random points, respectively. \mathbf{s}_c is dominated by the mean large-scale CMB gradient (henceforth we refer to this as the background), which is estimated by \mathbf{s}_r and corrected to obtain the final stacked dipole. To ensure that our background estimation is not biased due to sample variance, we set the value of $N_{\text{rand}} = 10 \times N_{\text{clus}}$. Here, we use the DES Y3 random catalogues which ensure that random points do not fall in the masked DES regions. The final stacked dipole is given by:

$$\mathbf{s} \equiv \mathbf{s}_c - \mathbf{s}_r = \frac{\sum_c^{N_{\text{clus}}} w_c [\mathbf{d}_c - \langle \mathbf{d}_c \rangle]}{\sum_c^{N_{\text{clus}}} w_c} - \frac{\sum_r^{N_{\text{rand}}} w_r [\mathbf{d}_r - \langle \mathbf{d}_r \rangle]}{\sum_r^{N_{\text{rand}}} w_r}, \quad (3.2)$$

where \mathbf{s} contains the dipole signal along with noise contributions from astrophysical and atmospheric foregrounds, instrumental noise, residual large-scale CMB gradient, the kSZ effect and in the case of temperature maps, the tSZ effect.

To remove the tSZ contribution from the stack (which could cause a bias toward lower masses if not taken into account), we follow the approach of [60] and rotate the cluster cutouts in random orientations prior to stacking. To ensure an accurate estimate of the tSZ contamination, we repeat this procedure 25 times and take the mean of the 25 stacks as our estimate of the tSZ signal. Fig. 3 illustrates the main steps involved in removing tSZ, with panel (a) showing our original stack (with tSZ contamination visible in the central pixels of the image), while panel (b) shows the mean of our 25 ‘random rotation’ stacks with an estimate of tSZ contamination. Finally, panel (c) shows our tSZ-free cluster stack which is obtained by subtracting the tSZ signal shown in panel (b) from panel (a).

¹Note that the Wiener filter is only applied to the larger cutouts of the tSZ-free map used for the gradient estimation step and the final $10' \times 10'$ rotated cutouts are extracted from an unfiltered SPT-3G map.

²This mean subtraction will ensure the mean of the pixels in the stacked cutout is equal to zero.

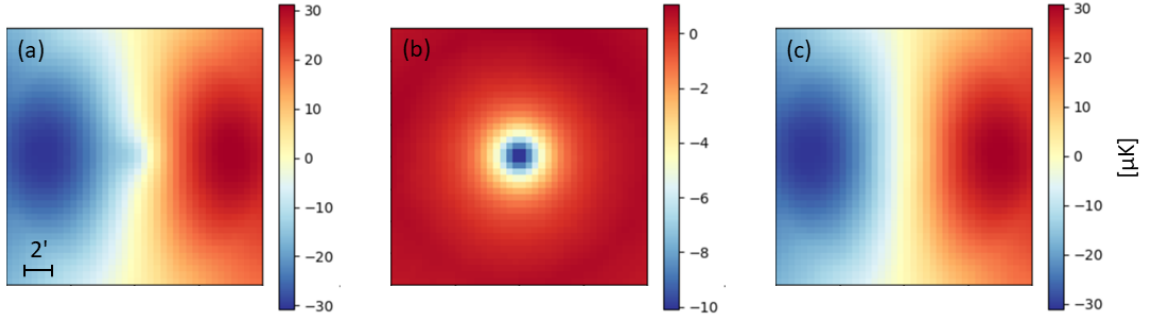


Figure 3. (a) The rotated and weighted cluster stack \mathbf{s}_c from our minimum variance temperature map, including the tSZ contamination. (b) The mean of 25 randomly rotated cluster stacks, with the tSZ signal visible at the centre of the cutout. (c) Panel (a)-(b): the final data stack after removing tSZ contamination.

3.2 Lensing dipole models

To create the lensing dipole models $\mathbf{m} \equiv \mathbf{m}(M)$, we generate noiseless cluster-lensed simulations for a set of N_{clus} clusters with the redshift distribution of the DES sample and cluster masses varying in the range $M \in [0, 4] \times 10^{14} M_{\odot}$ with linear bins of $\Delta M = 0.1 \times 10^{14} M_{\odot}$. For each mass bin, the N_{clus} cutouts are then stacked, following the steps in the previous section. Here, the mean background is simply given by $\mathbf{m}_r \equiv \mathbf{m}_c(M = 0)$ and is subtracted from the stacks in all mass bins. Since the uncertainties on the gradient direction ($\delta\theta_{\nabla}$) measurement will be lower in the case of noiseless simulations relative to the real data, the suboptimal stacking of the lensing dipole in the data compared to the models will cause a bias towards lower masses in the likelihoods, if not corrected for. For this reason, we add white noise and Gaussian foregrounds (mimicking those present in the data) to the models only when measuring $\delta\theta_{\nabla}$. In Section 3.4, we provide a more comprehensive description of the generated simulations, including the prescription for adding the impact of cluster miscentering and correlated structure to our modelled lensing profiles.

3.3 Stacked cluster mass likelihood

Equipped with the stacked dipole signal, \mathbf{s} , and the models, \mathbf{m} , we calculate the likelihood using

$$-2 \ln \mathcal{L}(M|\mathbf{s}) = \sum_{\text{pixels}} (\mathbf{s} - \mathbf{m}) \hat{\mathbf{C}}^{-1} (\mathbf{s} - \mathbf{m})^T, \quad (3.3)$$

where $\hat{\mathbf{C}}$ is the covariance matrix which is estimated from the data using the jackknife resampling technique by dividing the data into $N_{\text{jk}} = 0.9 N_{\text{clus}}$ subsamples:

$$\hat{\mathbf{C}} = \frac{N_{\text{jk}} - 1}{N_{\text{jk}}} \sum_{i=1}^{N_{\text{jk}}} [\mathbf{s}_i - \langle \mathbf{s} \rangle] [\mathbf{s}_i - \langle \mathbf{s} \rangle]^T. \quad (3.4)$$

Here, \mathbf{s}_i is the data stack in the i -th subsample and $\langle \mathbf{s} \rangle$ is the ensemble average of all subsamples. Estimating the covariance matrix from the data offers the advantage of capturing all sources of noise impacting the stacked lensing signal. When computing the likelihoods for our redshift and richness subsamples, which contain roughly one-third of the clusters from our Volume&Redshift-Limited sample, we adopt the covariance matrix derived from the latter and multiply it by a factor of 3 to account for the increased shot noise in the subsamples. This approach sidesteps potential inaccuracies

in estimating the covariance matrix that could result from using the smaller cluster samples from our redshift and richness subsamples.

3.4 Simulations & pipeline validation

In order to test the pipeline and estimate the expected S/N of our measurements, we follow a similar approach to [35] and create simulations of the lensed SPT-3G CMB temperature maps with properties similar to our minimum variance combination of the 95, 150, and 220 GHz maps from the real data. We generate a set of N_{clus} simulations by creating Gaussian realisations of the CMB in $60' \times 60'$ flat-sky maps. For each cluster, we model the convergence profile as $\kappa_{\text{tot}}(M, z) = \kappa_{1\text{h}}(M, z) + \kappa_{2\text{h}}(M, z)$. We model the one-halo term as a Navarro-Frenk-White [NFW; 61] profile, with the concentration parameter given by [62]. We account for the impact of uncertainties due to cluster miscentering following [63]:

$$\tilde{\kappa}_{1\text{h}}(\ell) = \kappa_{1\text{h}}(\ell) \left[(1 - f_{\text{mis}}) + f_{\text{mis}} \exp\left(-\frac{1}{2} \sigma_s^2 \ell^2\right) \right]. \quad (3.5)$$

Here, we use the DES miscentering fraction $f_{\text{mis}} = 0.22 \pm 0.11$ given by [59] and $\sigma_s = \sigma_R / D_A(z)$, where $D_A(z)$ is the angular diameter distance at the cluster redshift. The magnitude of miscentering is modelled as a Rayleigh distribution with $\sigma_R = c_{\text{mis}} R_\lambda$, where $R_\lambda = (\lambda/100)^{0.2} h^{-1} \text{Mpc}$ is the DES redMaPPer cluster radius, and $\ln c_{\text{mis}} = -1.13 \pm 0.22$ [see 23]. Following the approach of [48], we model the two-halo term, $\kappa_{2\text{h}}$, which takes into account the contribution of correlated structures to the total lensing convergence, following Equation (13) of [64]. We convolve the CMB maps with the SPT-3G 150 GHz beam function [54] and add the noise measured from our minimum variance combination of the 95, 150, and 220 GHz maps from the real data. We also include cluster tSZ and kSZ signals based on the Agora simulation set [65] and include the foreground power due to CIB and radio galaxies based on measurements by [66]. To mimic the impact of filtering applied to the data during the map-making process, we follow previous works (including [35]; [45]) and apply a 2D transfer function of the form $F_{\vec{\ell}} = e^{-(\ell_1/\ell_x)^6} e^{-(\ell_x/\ell_2)^6}$, with $\ell_1 = 300$ and $\ell_2 = 13000$ to the simulations.

The central $10' \times 10'$ region of each simulation is then extracted and processed through the pipeline as described in Sections 3.1 and 3.2 for the simulated data and models, respectively. For the purpose of pipeline verification, we generated 25 sets of mock CMB cluster lensed simulations each with N_{clus} , one set of random CMB simulation with $N_{\text{rand}} = 10 \times N_{\text{clus}}$ and 25 sets of model simulations per mass bin, each with N_{clus} lensed clusters. In the case of the 25 mock simulation sets, we estimated a unique jackknife covariance matrix for each simulation set and set $N_{\text{clus}} = 5500$, roughly matching the number of clusters in the DES-Y3 Volume-Limited sample described in Section 2.3. For each simulated cluster, we assign the mass and redshift corresponding to a real cluster in the DES-Y3 sample. In the case of the models, where the cluster masses are fixed in each mass bin, we set the redshift distribution of the clusters to that of the DES-Y3 sample. To convert the cluster richness to cluster mass, we use the $M - \lambda$ scaling relation based on the weak lensing analysis of [47] given by $\langle M_{200\text{m}} | \lambda, z \rangle = 3.081 \times 10^{14} (\lambda/40)^{1.356} ((1+z)/1.35)^{-0.3}$, resulting in a mean mass of $M_{200\text{m}} = 2.21 \times 10^{14} M_\odot$ for the DES Volume&Redshift-Limited cluster sample used in this analysis. We then evaluate the significance of our lensing measurement using $S/N = \sqrt{2[\ln \mathcal{L}(M_{200\text{m}} = M_{\text{DES}}) - \ln \mathcal{L}(M_{200\text{m}} = 0)]}$, where M_{DES} is our measured stacked mass of the DES cluster sample.

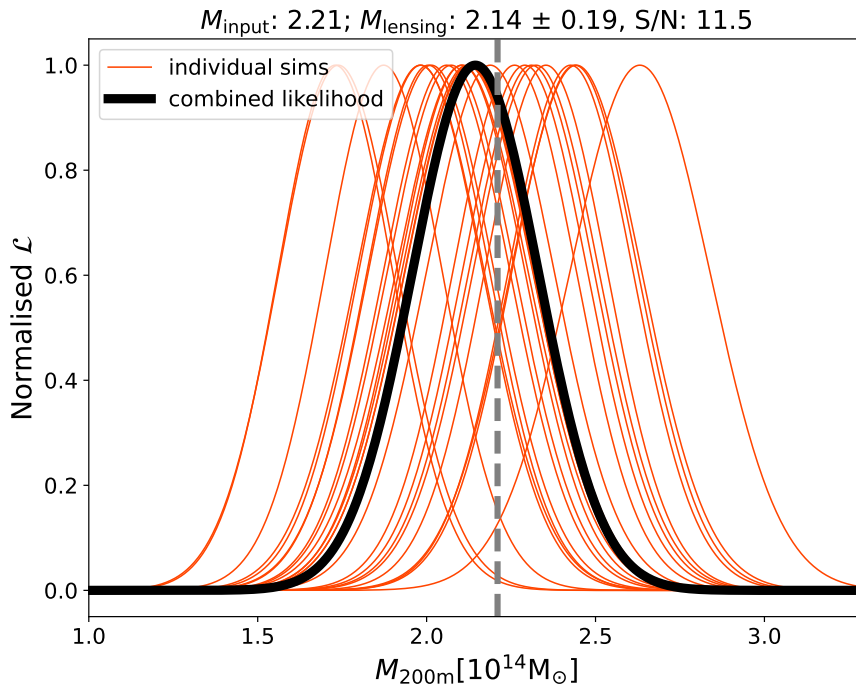


Figure 4. Likelihoods showing the results of the pipeline test for 25 sets of simulations (thin orange curves) described in Section 3.4 and their combined likelihood (thick black curves). For the combined likelihood, the width of the distribution is scaled up by a factor of 5 in order to demonstrate the expected S/N from one simulation run with the same number of clusters as our real data. The dashed vertical line is the mean cluster mass of the input sample used to produce the lensing simulations. We find a good agreement between the input mass and the recovered mass.

4 Results and Discussion

4.1 Pipeline verification results

Figure 4 shows the result of our pipeline verification test based on 25 sets of simulations (shown as thin orange curves). The thick black curve shows the combined likelihood with the standard deviation multiplied by a factor of $\sqrt{25}$, to estimate the S/N expected from a cluster dataset with the mass and redshift distribution of the DES Volume-Limited sample. The dashed vertical line represents the mean mass of the cluster sample ($2.21 \times 10^{14} M_{\odot}$) and we find that the pipeline successfully recovers the expected mass of the input sample.

The successful pipeline validation indicates that the intrinsic richness scatter of the DES sample does not have a significant impact on measuring the mean cluster mass of the sample. Furthermore, the pipeline test indicates the validity of the assumption that, by measuring the mean lensing signal, we can measure the mean cluster mass.

4.2 Mean cluster mass

Our CMB cluster lensing measurement results in a mean (stacked) cluster mass of

$$\begin{aligned}
 M_{200m} &= 1.66 \pm 0.13 \text{ [stat.]} \pm 0.03 \text{ [sys.]} \times 10^{14} M_{\odot} \quad (8.6\%), \\
 M_{200m} &= 1.97 \pm 0.18 \text{ [stat.]} \pm 0.05 \text{ [sys.]} \times 10^{14} M_{\odot} \quad (10.2\%), \\
 M_{200m} &= 2.11 \pm 0.20 \text{ [stat.]} \pm 0.05 \text{ [sys.]} \times 10^{14} M_{\odot} \quad (10.4\%).
 \end{aligned}$$

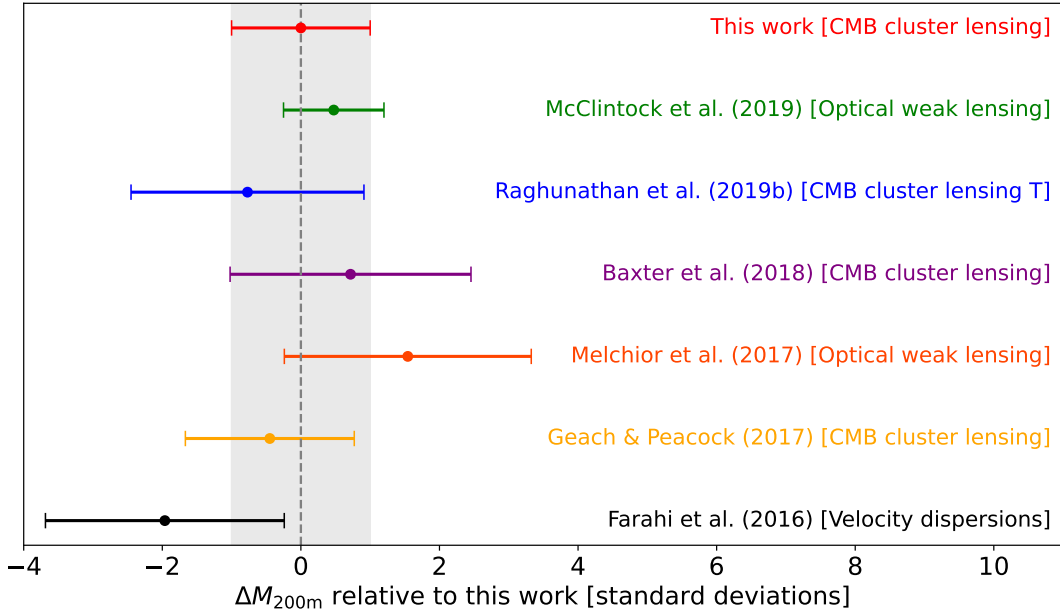


Figure 5. Comparison of the measured mean cluster mass of this work (Volume&Redshift-Limited sample) and the mean cluster mass of the same sample, based on the redMaPPer cluster mass–richness scaling relations of various other studies.

for the DES-Y3 Flux-, Volume-, and Volume&Redshift-Limited samples, respectively. These are the most constraining mass measurements obtained from CMB cluster lensing to date.

Figure 5 shows a comparison of the mean cluster mass for our Volume&Redshift-Limited sample and the mean cluster mass of the same sample based on the mass–richness scaling relations of [47], [23] (calibrated using optical weak lensing), [52], [45] and [44] (calibrated using CMB cluster lensing) and [67] (calibrated using spectroscopic velocity dispersion measurement of cluster galaxies). For ease of comparison, all measurements are normalised relative to this work with the shaded region marking the 1σ uncertainty on our measurement. Overall, we find a good agreement between our measurement of the mean cluster mass and the results of other studies.

4.3 Systematics

In this section, we explore contributions from beam uncertainties, transfer function modelling, residual foregrounds, and cluster miscentering to the systematic error budget. We focus on these sources of systematics, as they have been shown to dominate systematic uncertainty in previous works (see Section 4.2 of [48]). Here, we ignore systematic contributions from underlying cosmology and the choice of halo profile, as these have been found to be small in previous analyses (see [48], [45]) and negligible given the current magnitude of statistical uncertainty. However, quantification of these systematics will become important in future experiments such as CMB-S4, where the statistical uncertainty is expected to be reduced to 1% given the much larger sample size of $\sim 100,000$ clusters.

4.3.1 Cluster tSZ Signal and Residual Foregrounds

The tSZ signal is an important source of systematics, which could result in a bias towards lower masses if not correctly accounted for. In order to verify the success of the random rotation method

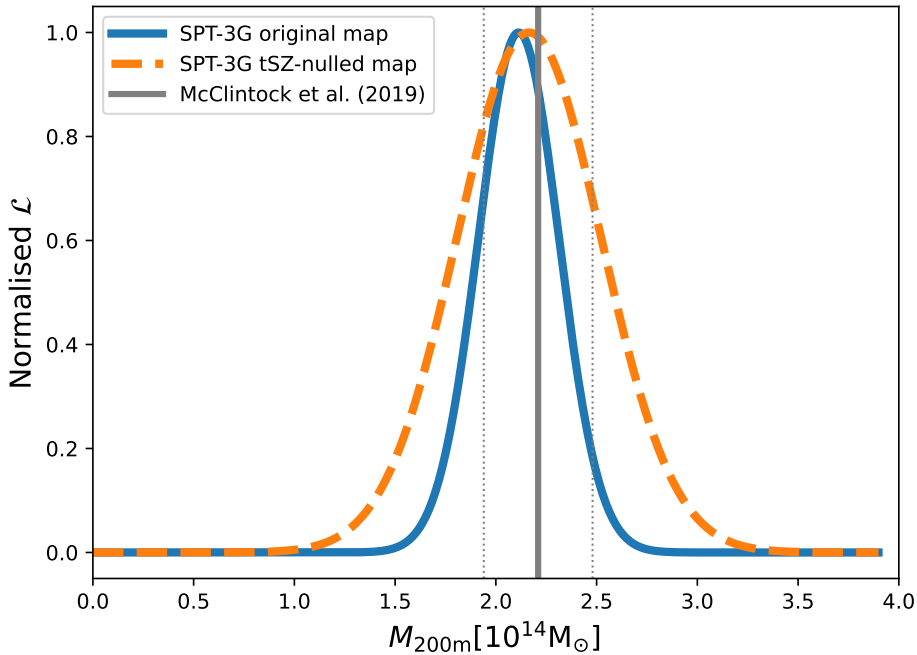


Figure 6. Comparison of mass likelihoods obtained using the SPT-3G tSZ-nulled temperature map (dashed orange curve) and our original maps (solid blue curve) in which the tSZ signal is estimated using random rotations and removed from the lensing stack. For comparison, we also include mean sample mass based on the optical weak lensing calibrated, mass–richness scaling relation of [47] (solid vertical line with the 1σ error region indicated by the horizontal dotted lines).

(described in Section 3.1) in removing the tSZ signal from our stacked lensing dipole, we repeat the measurement using the tSZ-nulled minimum-variance map, described in Section 2.2, for our Volume&Redshift-Limited sample.

Figure 6 shows a comparison of the mass likelihoods obtained from either the baseline minimum variance map or the more noisy tSZ-nulled minimum variance map, with the two appearing in good agreement. Nulling the tSZ signal significantly increases the map variance, primarily due to the CIB and instrumental noise terms. Thus using the tSZ-nulled map approximately doubles the mass uncertainty compared to the baseline case where the tSZ signal is removed by the random rotation stacking procedure. We choose to proceed with the baseline map.

The success of the random rotation technique in mitigating tSZ contamination has also been verified using a larger sample of simulated clusters, in previous studies [35, 60]. Similarly, we use the simulations described in Section 3.4, to estimate the contribution from residual tSZ and kSZ, as well as foregrounds due to CIB and radio galaxies, to our systematic error. This is done by running our pipeline based on a simulation set without foregrounds, tSZ, and kSZ signals, and then repeating the run on the same simulation set with the tSZ, kSZ, and foregrounds added in. Based on this test, we find a contribution of 1.3% to our error budget, equivalent to a shift of 0.12σ in our results.

4.3.2 Cluster miscentering

To estimate the systematic uncertainty due to our cluster miscentering model, we repeat the cluster mass measurement for the Volume&Redshift-Limited sample with our fiducial setup but change the miscentering parameters by their 1σ uncertainty to $f_{\text{mis}} = 0.30$ (see [47]) and $\ln c_{\text{mis}} = -1.35$. In this

Source of Error	Magnitude of Error	frac. of σ_{stat}
Cluster miscentering	1.7%	0.15σ
Beam uncertainties	1.7%	0.15σ
Residual foregrounds	1.3%	0.12σ
Filtering model	0.9%	0.07σ
Total	2.4%	0.25σ

Table 2. Systematic Error Budget in the Stacked Mass for DES RM Year 3 Volume&redshift-limited Sample

case, the measured mean cluster mass increases by 1.7% or 0.15σ .³

4.3.3 Filtering model

As described in Section 3.4, we estimate the impact of filtering applied to our CMB maps using a 2D transfer function with high- and low-pass filter components set to $\ell_1 = 300$ and $\ell_2 = 13000$ respectively. While ℓ_2 is set to angular scales that do not matter to our lensing reconstruction, we need to calculate the systematics due to the uncertainty on the position of the high-pass filter $\ell_1 = 300 \pm 20$. To this end, we recompute our models assuming $\ell_1 = 280$ and 320 and evaluate the changes in the mean lensing mass of our Volume&Redshift-Limited sample. Based on this analysis, we find the systematic contribution of our filtering model to be 0.9% (or 0.07σ).

4.3.4 Beam uncertainties

To estimate the uncertainties in our modelling of the telescope beam profile, we generate 10 Gaussian realisations of the beam and regenerate our models of the lensing dipole (described in Section 3.2) for these beams. To generate the simulated beams, we take the beam covariance matrix $\Sigma_{\ell\ell'} = \langle \delta B_\ell \delta B_{\ell'} \rangle$, with δB_ℓ denoting the deviation of B_ℓ from its mean \bar{B}_ℓ . Here, the elements of the covariance matrix are given by $\Sigma_{\ell\ell'} = (Q\Lambda Q^\top)_{\ell\ell'}$, where, the diagonal matrix Λ contains the eigenvalues λ_i of the covariance matrix, and the orthogonal matrix Q , contains the eigenvectors v_i of the covariance matrix, satisfying $\Sigma v_i = \lambda_i v_i$.

Under the assumption that $\Sigma_{\ell\ell'}$ encapsulates the statistical characteristics of the beam (i.e., the relevant coefficients follow a Gaussian distribution), we can simulate beam profiles as follows:

$$\hat{B}_\ell = \bar{B}_\ell + a_{i\ell} e_{i\ell},$$

where $e_{i\ell}$ represents the ℓ th component of the i th column in $Q\sqrt{\Lambda}$, and a_i are standard Gaussian variables with zero mean and unit variance $\langle a_i a_j \rangle = \delta_{ij}$.

We then repeat our measurement of the mean cluster mass for the Volume&Redshift-Limited sample and take the 1σ uncertainty on these 10 new measurements as our estimate of the systematic uncertainty due to our beam modelling. Here, we find a 1.7% contribution to our systematic error budget, equivalent to 0.15σ of our statistical error. We provide a summary of the different contributors to our systematic error budget in Table 2.

4.3.5 Optical weak lensing systematics

In this work, we perform direct comparisons of our results with cluster masses given by the optical weak lensing calibrated mass–richness scaling relation of [47]. As such, we present a brief discussion

³We note that if one uses a larger uncertainty on f_{mis} (e.g. based on the [59] estimate from the smaller DES Science Verification sample) and takes $f_{\text{mis}} = 0.33$, the result changes by $\sim 3.4\%$ ($\sim 0.29\sigma$).

of systematics impacting optical weak lensing analyses, as well as outstanding cosmological tensions between analyses of the DES Y1 cluster sample and various other cosmological probes.

The constraints on Ω_m and σ_8 from a joint cluster abundances and weak lensing analysis of the DES Y1 cluster sample are in 2.4σ tension with the DES Y1 3×2 pt results, and in 5.6σ with the Planck CMB analysis [68]. The weak lensing measurements used in this analysis were based on the results of [47], where the systematic uncertainty was estimated to be 4.3%. As such, weak lensing mass calibration systematics alone are not sufficient to explain the tensions found in the analysis of [68].

In a later work, [69] explored the contamination of the DES-Y1 cluster sample with SPT-SZ selected clusters. Here, it was shown that 10 – 20% of the $\lambda < 40$ DES redMaPPer clusters are galaxy groups with masses of $\sim 3 - 5 \times 10^{13} M_\odot$ that are misclassified as more massive clusters due to projection effects. The presence of such low-mass systems in the DES Y1 sample is likely a dominant contributing factor to the cosmological tensions presented in [68]. Indeed, it was shown in [68], that tensions can be significantly alleviated by limiting the sample to clusters with $\lambda \geq 30$, which further supports this hypothesis.

It is important to note that systematics due to the presence of such low-mass contaminants will also bias the CMB lensing measurements presented in this study, and in the future, more work is needed to better characterise and minimise the impact of such contaminants via spectroscopic follow-up, use of different cluster detection algorithms, and comparison to future X-ray and SZ samples which probe lower cluster masses.

4.4 Cluster mass–richness scaling relation

In Figure 7, we compare our binned cluster mass measurements with those given by the mass–richness scaling relation of [47]. We find good agreement between the CMB cluster lensing and optical weak lensing measurements across all richness bins. Based on fitting a two-parameter model (with no redshift evolution), to the cluster mass measurements in our three richness bins, we obtain a mass–richness scaling relation given by:

$$M_{200m} = [3.0 \pm 0.4] \times 10^{14} M_\odot (\lambda/40)^{1.6 \pm 0.5}. \quad (4.1)$$

This best-fit model has a chi-square value of 2.59 (p -value of 0.11). We note that the constraining power of the current data limits us to 3 richness bins, which matches the number of free parameters in the [47] model. As such, we are unable to perform statistical tests to quantitatively assess the level of agreement between our data and the [47] scaling relation which contains 3 free parameters, and leave this to future analyses.

4.5 Mean cluster mass as a function of redshift

Figure 8 shows the mean cluster mass for three redshift sub-samples of our Volume&Redshift-Limited sample described in Table 1. The red data points show the measurements from this work compared to the mean masses of the same subsamples (blue data points), obtained using the optical weak lensing calibrated mass–richness scaling relation of [47]. We find a reasonable agreement between the measurements, noting only a $\sim 1.7\sigma$ deviation between the two measurements in the lowest redshift bin. As this modest divergence is not statistically significant, we do not investigate it further at this stage. However, it would be interesting to see if such a discrepancy persists in future SPT-3G measurements at a higher level of statistical significance.

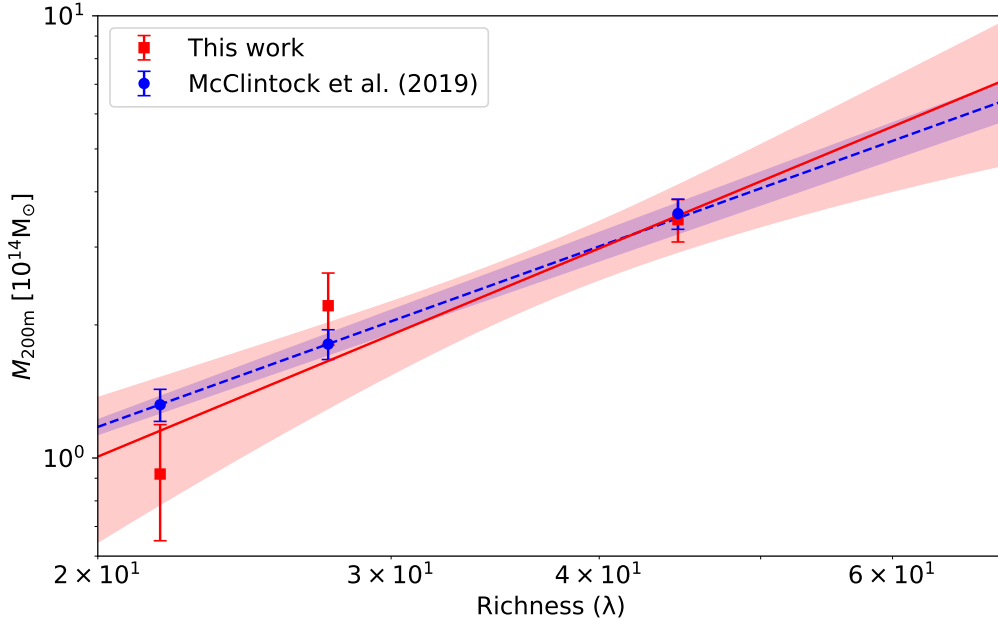


Figure 7. Mass–richness scaling relation fitted to our measured cluster masses of the Volume&Redshift-Limited sample in three richness bins (red squares/solid line), compared to the cluster masses given by the mass–richness scaling relation of [47] (blue circles/dashed line). The shaded regions indicate the 1σ uncertainty of the scaling relations.

SPT-3G survey field	Data	Years observed	Map depth [$\mu\text{K}\cdot\text{arcmin}$]	DES overlap [deg^2]	Mass constraint [%]
Main (This work)	T	2019+20	3.1	1350	10.4
Main	T	2019-23, 2025-26	1.6	1350	7.4
Main	T+Pol	2019-23, 2025-26	1.6	1350	6.6
Extended	T+Pol	2019-23	6.1	1420	12.6
Main+Extended	T+Pol	–	–	2770	5.8

Table 3. Mass constraint forecasts with the addition of various SPT-3G survey data. Here, the map depth is given by the inverse quadrature sum of the noise in the 95, 150 and 220 GHz frequency bands.

4.6 Forecasts

In this section, we provide forecasts for the expected mass constraints one could achieve by including polarization data and upon the completion of the SPT-3G survey, including data from the SPT-3G ‘Extended’ survey (providing a total of $\sim 2800 \text{ deg}^2$ overlap with DES, albeit at varying sensitivities). We summarise these forecasts in Table 3. Here, we can see that upon completion of the survey in 2026 and by including polarization and the Extended survey observations, we can improve the current mass constraints by a factor of ~ 1.8 , obtaining a 5.8% stacked cluster mass constraint. This is much more competitive with optical weak lensing mass constraints and will allow for more precise cosmological parameter estimation.

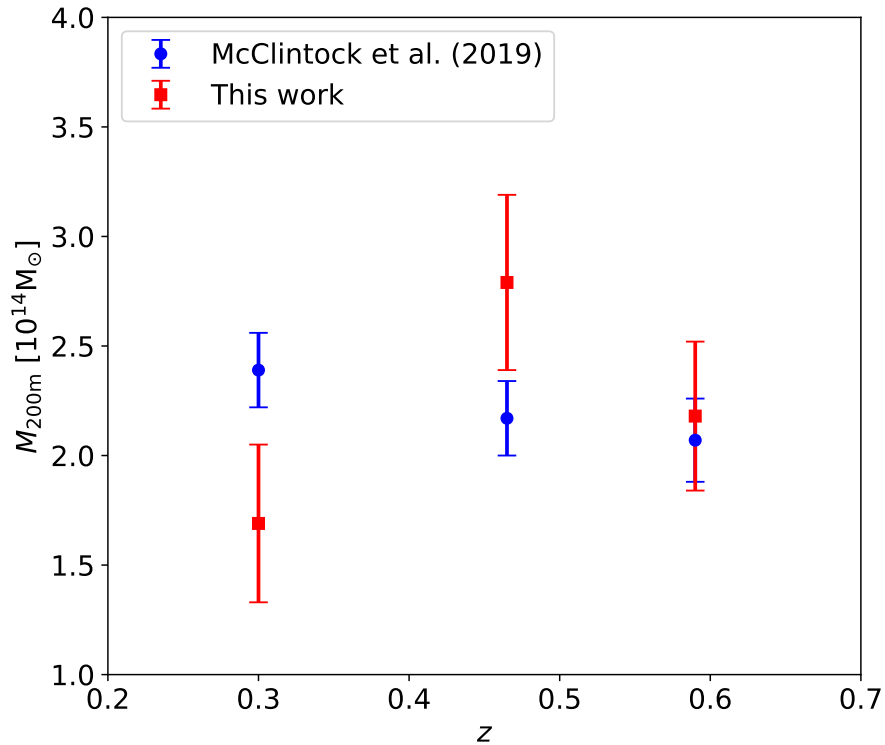


Figure 8. Comparison of the mean cluster mass measurements of this work for three redshift bins, to masses based on the optical weak lensing calibrated, mass–richness scaling relation of [47].

5 Conclusions

In this study, we presented a measurement of the mean cluster masses of three DES-Y3 galaxy cluster samples using the CMB cluster lensing measurements from the initial two years of observations of the SPT-3G survey. Here, we restrict our measurements to the temperature data and the ‘Main’ SPT-3G survey which has a 1350 deg² overlap with DES (after masking) and leave the addition of SPT-3G polarization maps, as well as data from the SPT-3G ‘Extended’ survey to future works when additional SPT-3G observations are available.

The DES-Y3 cluster samples used in this analysis consist of a Flux-Limited sample with 8865 clusters, a Volume-Limited sample with 5391 clusters and a Volume&Redshift-Limited sample with 4450 clusters. The latter sample is designed to match the selection function of the cluster sample used for DES cluster cosmology analyses, and thus is the primary focus of this work. For the three samples, we detect the CMB lensing dipole with a significance of 10.3 σ , 10.0 σ and 9.6 σ and find the mean cluster masses to be:

$$\begin{aligned}
 M_{200m} &= 1.66 \pm 0.13 \text{ [stat.]} \pm 0.03 \text{ [sys.]} \times 10^{14} M_{\odot} \quad (8.6\%), \\
 M_{200m} &= 1.97 \pm 0.18 \text{ [stat.]} \pm 0.05 \text{ [sys.]} \times 10^{14} M_{\odot} \quad (10.2\%), \\
 M_{200m} &= 2.11 \pm 0.20 \text{ [stat.]} \pm 0.05 \text{ [sys.]} \times 10^{14} M_{\odot} \quad (10.4\%).
 \end{aligned}$$

This measurement represents a factor of ~ 2 improvement in precision relative to CMB cluster lensing measurements based on previous generations of SPT surveys (see, e.g. [45], [48] and [35])

and is much more competitive with optical weak lensing mass constraints. Overall, we find good agreement between our measurements and those given by the redMaPPer mass–richness scaling relations of previous works (e.g. [67], [44], [23], [45], [48] and [47]) calibrated using techniques including CMB cluster lensing, optical weak-lensing, and velocity dispersion measurements from various combinations of DES, SDSS, and Planck data.

We verify that our measurements are not significantly biased due to contamination from the residual tSZ signal by comparing the mass of our Volume&Redshift-Limited sample to the mass of the same sample obtained using CMB cluster lensing of a tSZ-nulled ILC map. We find a good agreement between the two measurements, with the higher noise levels in the tSZ-nulled map resulting in a factor of ~ 2 larger uncertainty on the mean cluster mass.

Although it was not possible to measure cluster masses for different redshift and richness bins in previous SPT works due to the low S/N of the lensing dipole, the improved sensitivity of the SPT-3G data and the greater overlap with DES enables us to divide our Volume&Redshift-Limited sample into 3 redshift and richness bins, each containing $\sim 1/3$ of the clusters in the full sample. For these subsamples, we obtain mass constraints ranging from 10 – 20% in precision (with a mean precision of 14%). Our results across these sub-samples do not reveal any significant discrepancies when compared to the optical weak lensing calibrated masses given by the scaling relation of [47], although we observe that our mass measurement in the lowest redshift bin is $\sim 1.7\sigma$ lower.

Finally, we perform forecasts for expected mass constraints using various combinations of the upcoming SPT-3G data. We find that upon completion of the survey in 2026, the combination of temperature and polarization data would yield mass constraints of 6.6% and 12.6% in the Main and Extended SPT-3G surveys, respectively, which translates to a 5.8% mass constraint upon the combination of the full SPT-3G datasets. This level of precision will make CMB cluster lensing much more competitive with optical weak lensing in future years. Moreover, it will serve as an important test of the robustness of cluster mass measurements for precision cosmology due to the complementary systematics of the two measurements.

Acknowledgments

The Melbourne team acknowledges support from the Australian Research Council’s Discovery Projects scheme (DP200101068).

SR acknowledges support from the Center for AstroPhysical Surveys (CAPS) at the National Center for Supercomputing Applications (NCSA), University of Illinois Urbana-Champaign.

The South Pole Telescope program is supported by the National Science Foundation (NSF) through award OPP-1852617. Partial support is also provided by the Kavli Institute of Cosmological Physics at the University of Chicago.

This project has received funding from the European Research Council (ERC) under the European Union’s Horizon 2020 research and innovation programme (grant agreement No 101001897)

Funding for the DES Projects has been provided by the U.S. Department of Energy, the U.S. National Science Foundation, the Ministry of Science and Education of Spain, the Science and Technology Facilities Council of the United Kingdom, the Higher Education Funding Council for England, the National Center for Supercomputing Applications at the University of Illinois at Urbana-Champaign, the Kavli Institute of Cosmological Physics at the University of Chicago, the Center for Cosmology and Astro-Particle Physics at the Ohio State University, the Mitchell Institute for Fundamental Physics and Astronomy at Texas A&M University, Financiadora de Estudos e Projetos, Fundação Carlos Chagas Filho de Amparo à Pesquisa do Estado do Rio de Janeiro, Conselho Nacional

de Desenvolvimento Científico e Tecnológico and the Ministério da Ciência, Tecnologia e Inovação, the Deutsche Forschungsgemeinschaft and the Collaborating Institutions in the Dark Energy Survey.

The Collaborating Institutions are Argonne National Laboratory, the University of California at Santa Cruz, the University of Cambridge, Centro de Investigaciones Energéticas, Medioambientales y Tecnológicas-Madrid, the University of Chicago, University College London, the DES-Brazil Consortium, the University of Edinburgh, the Eidgenössische Technische Hochschule (ETH) Zürich, Fermi National Accelerator Laboratory, the University of Illinois at Urbana-Champaign, the Institut de Ciències de l’Espai (IEEC/CSIC), the Institut de Física d’Altes Energies, Lawrence Berkeley National Laboratory, the Ludwig-Maximilians Universität München and the associated Excellence Cluster Universe, the University of Michigan, NSF’s NOIRLab, the University of Nottingham, The Ohio State University, the University of Pennsylvania, the University of Portsmouth, SLAC National Accelerator Laboratory, Stanford University, the University of Sussex, Texas A&M University, and the OzDES Membership Consortium.

Based in part on observations at Cerro Tololo Inter-American Observatory at NSF’s NOIRLab (NOIRLab Prop. ID 2012B-0001; PI: J. Frieman), which is managed by the Association of Universities for Research in Astronomy (AURA) under a cooperative agreement with the National Science Foundation.

The DES data management system is supported by the National Science Foundation under Grant Numbers AST-1138766 and AST-1536171. The DES participants from Spanish institutions are partially supported by MICINN under grants ESP2017-89838, PGC2018-094773, PGC2018-102021, SEV-2016-0588, SEV-2016-0597, and MDM-2015-0509, some of which include ERDF funds from the European Union. IFAE is partially funded by the CERCA program of the Generalitat de Catalunya. Research leading to these results has received funding from the European Research Council under the European Union’s Seventh Framework Program (FP7/2007-2013) including ERC grant agreements 240672, 291329, and 306478. We acknowledge support from the Brazilian Instituto Nacional de Ciência e Tecnologia (INCT) do e-Universo (CNPq grant 465376/2014-2).

This manuscript has been authored by Fermi Research Alliance, LLC under Contract No. DE-AC02-07CH11359 with the U.S. Department of Energy, Office of Science, Office of High Energy Physics.

Argonne National Laboratory’s work was supported by the U.S. Department of Energy, Office of High Energy Physics, under Contract No. DE- AC02-06CH11357.

We acknowledge the use of <http://astromap.icrar.org/> for producing Fig. 1. Some of the results in this paper have been derived using the HEALPY [70] and HEALPIX [71] packages. The analysis of this work also made use of PYTHON3 [72] and packages including SCIPY [73], NUMPY [74], ASTROPY [75] and PANDAS [76].

References

- [1] S.W. Allen, A.E. Evrard and A.B. Mantz, *Cosmological Parameters from Observations of Galaxy Clusters*, *ARA&A* **49** (2011) 409 [1103.4829].
- [2] D.H. Weinberg, M.J. Mortonson, D.J. Eisenstein, C. Hirata, A.G. Riess and E. Rozo, *Observational probes of cosmic acceleration*, *PhR* **530** (2013) 87 [1201.2434].
- [3] P. Schuecker, R.R. Caldwell, H. Böhringer, C.A. Collins, L. Guzzo and N.N. Weinberg, *Observational constraints on general relativistic energy conditions, cosmic matter density and dark energy from X-ray clusters of galaxies and type-Ia supernovae*, *A&A* **402** (2003) 53 [astro-ph/0211480].
- [4] L. Salvati, M. Douspis and N. Aghanim, *Constraints from thermal Sunyaev-Zel’dovich cluster counts and power spectrum combined with CMB*, *A&A* **614** (2018) A13 [1708.00697].

- [5] Planck Collaboration, P.A.R. Ade, N. Aghanim, M. Arnaud, M. Ashdown, J. Aumont et al., *Planck 2015 results. XXIV. Cosmology from Sunyaev-Zeldovich cluster counts*, *A&A* **594** (2016) A24 [[1502.01597](#)].
- [6] S. Bocquet, J.P. Dietrich, T. Schrabback, L.E. Bleem, M. Klein, S.W. Allen et al., *Cluster Cosmology Constraints from the 2500 deg² SPT-SZ Survey: Inclusion of Weak Gravitational Lensing Data from Magellan and the Hubble Space Telescope*, *ApJ* **878** (2019) 55 [[1812.01679](#)].
- [7] B. Ansarinejad and T. Shanks, *Detection significance of baryon acoustic oscillations peaks in galaxy and quasar clustering*, *MNRAS* **479** (2018) 4091.
- [8] S. Alam, M. Aubert, S. Avila, C. Balland, J.E. Bautista, M.A. Bershadsky et al., *Completed SDSS-IV extended Baryon Oscillation Spectroscopic Survey: Cosmological implications from two decades of spectroscopic surveys at the Apache Point Observatory*, *PhRvD* **103** (2021) 083533.
- [9] Planck Collaboration, N. Aghanim, Y. Akrami, M. Ashdown, J. Aumont, C. Baccigalupi et al., *Planck 2018 results. VI. Cosmological parameters*, *A&A* **641** (2020) A6 [[1807.06209](#)].
- [10] S. Aiola, E. Calabrese, L. Maurin, S. Naess, B.L. Schmitt, M.H. Abitbol et al., *The Atacama Cosmology Telescope: DR4 maps and cosmological parameters*, *JCAP* **2020** (2020) 047.
- [11] L. Balkenhol, D. Dutcher, A. Spurio Mancini, A. Doussot, K. Benabed, S. Galli et al., *Measurement of the CMB temperature power spectrum and constraints on cosmology from the SPT-3G 2018 TT, TE, and EE dataset*, *PhRvD* **108** (2023) 023510 [[2212.05642](#)].
- [12] T.M.C. Abbott, M. Aguena, A. Alarcon, S. Allam, O. Alves, A. Amon et al., *Dark Energy Survey Year 3 results: Cosmological constraints from galaxy clustering and weak lensing*, *PhRvD* **105** (2022) 023520 [[2105.13549](#)].
- [13] C. Heymans, T. Tröster, M. Asgari, C. Blake, H. Hildebrandt, B. Joachimi et al., *KiDS-1000 Cosmology: Multi-probe weak gravitational lensing and spectroscopic galaxy clustering constraints*, *A&A* **646** (2021) A140 [[2007.15632](#)].
- [14] H. Miyatake, S. Sugiyama, M. Takada, T. Nishimichi, X. Li, M. Shirasaki et al., *Hyper Suprime-Cam Year 3 results: Cosmology from galaxy clustering and weak lensing with HSC and SDSS using the emulator based halo model*, *PhRvD* **108** (2023) 123517 [[2304.00704](#)].
- [15] T.M.C. Abbott, F.B. Abdalla, J. Annis, K. Bechtol, J. Blazek, B.A. Benson et al., *Dark Energy Survey Year 1 Results: A Precise H₀ Estimate from DES Y1, BAO, and D/H Data*, *MNRAS* **480** (2018) 3879 [[1711.00403](#)].
- [16] A. Merloni, P. Predehl, W. Becker, H. Böhringer, T. Boller, H. Brunner et al., *eROSITA Science Book: Mapping the Structure of the Energetic Universe*, *ArXiv e-prints* (2012) [[1209.3114](#)].
- [17] Ž. Ivezić, S.M. Kahn, J.A. Tyson, B. Abel, E. Acosta, R. Allsman et al., *LSST: From Science Drivers to Reference Design and Anticipated Data Products*, *ApJ* **873** (2019) 111 [[0805.2366](#)].
- [18] R. Laureijs, J. Amiaux, S. Arduini, J. Auguères, J. Brinchmann, R. Cole et al., *Euclid Definition Study Report*, *ArXiv e-prints* (2011) [[1110.3193](#)].
- [19] K.N. Abazajian, P. Adshead, Z. Ahmed, S.W. Allen, D. Alonso, K.S. Arnold et al., *CMB-S4 Science Book, First Edition*, *arXiv e-prints* (2016) arXiv:1610.02743 [[1610.02743](#)].
- [20] K. Umetsu, *Cluster-galaxy weak lensing*, *A&A Rv* **28** (2020) 7.
- [21] D.E. Applegate, A. von der Linden, P.L. Kelly, M.T. Allen, S.W. Allen, P.R. Burchat et al., *Weighing the Giants – III. Methods and measurements of accurate galaxy cluster weak-lensing masses*, *Monthly Notices of the Royal Astronomical Society* **439** (2014) 48 [<https://academic.oup.com/mnras/article-pdf/439/1/48/5560953/stt2129.pdf>].
- [22] M. Simet, T. McClintock, R. Mandelbaum, E. Rozo, E. Rykoff, E. Sheldon et al., *Weak lensing measurement of the mass–richness relation of SDSS redMaPPer clusters*, *Monthly Notices of the Royal Astronomical Society* **466** (2016) 3103 [<https://academic.oup.com/mnras/article-pdf/466/3/3103/10903108/stw3250.pdf>].

- [23] P. Melchior, D. Gruen, T. McClintock, T.N. Varga, E. Sheldon, E. Rozo et al., *Weak-lensing mass calibration of redMaPPer galaxy clusters in Dark Energy Survey Science Verification data*, *MNRAS* **469** (2017) 4899 [[1610.06890](#)].
- [24] S. Grandis, S. Bocquet, J.J. Mohr, M. Klein and K. Dolag, *Calibration of bias and scatter involved in cluster mass measurements using optical weak gravitational lensing*, *MNRAS* **507** (2021) 5671 [[2103.16212](#)].
- [25] S. Bocquet, S. Grandis, L.E. Bleem, M. Klein, J.J. Mohr, M. Aguena et al., *SPT Clusters with DES and HST Weak Lensing. I. Cluster Lensing and Bayesian Population Modeling of Multi-Wavelength Cluster Datasets*, *arXiv e-prints* (2023) arXiv:2310.12213 [[2310.12213](#)].
- [26] U. Seljak and M. Zaldarriaga, *Lensing-induced Cluster Signatures in the Cosmic Microwave Background*, *ApJ* **538** (2000) 57 [[astro-ph/9907254](#)].
- [27] W. Hu, S. DeDeo and C. Vale, *Cluster mass estimators from CMB temperature and polarization lensing*, *New Journal of Physics* **9** (2007) 441 [[astro-ph/0701276](#)].
- [28] S. Raghunathan, N. Whitehorn, M.A. Alvarez, H. Aung, N. Battaglia, G.P. Holder et al., *Constraining Cluster Virialization Mechanism and Cosmology Using Thermal-SZ-selected Clusters from Future CMB Surveys*, *ApJ* **926** (2022) 172 [[2107.10250](#)].
- [29] G. Holder and A. Kosowsky, *Gravitational Lensing of the Microwave Background by Galaxy Clusters*, *ApJ* **616** (2004) 8 [[astro-ph/0401519](#)].
- [30] M. Maturi, M. Bartelmann, M. Meneghetti and L. Moscardini, *Gravitational lensing of the CMB by galaxy clusters*, *A&A* **436** (2005) 37 [[astro-ph/0408064](#)].
- [31] A. Lewis and L. King, *Cluster masses from CMB and galaxy weak lensing*, *PhRvD* **73** (2006) 063006 [[astro-ph/0512104](#)].
- [32] J. Yoo, M. Zaldarriaga and L. Hernquist, *Lensing reconstruction of cluster-mass cross correlation with cosmic microwave background polarization*, *Phys. Rev. D* **81** (2010) 123006.
- [33] J.-B. Melin and J.G. Bartlett, *Measuring cluster masses with CMB lensing: a statistical approach*, *A&A* **578** (2015) A21 [[1408.5633](#)].
- [34] B. Horowitz, S. Ferraro and B.D. Sherwin, *Reconstructing small-scale lenses from the cosmic microwave background temperature fluctuations*, *MNRAS* **485** (2019) 3919 [[1710.10236](#)].
- [35] S. Raghunathan, S. Patil, E. Baxter, B.A. Benson, L.E. Bleem, T.M. Crawford et al., *Detection of CMB-Cluster Lensing using Polarization Data from SPTpol*, *PhRvL* **123** (2019) 181301 [[1907.08605](#)].
- [36] S. Saha, L. Legrand and J. Carron, *Cluster profiles from beyond-the-QE CMB lensing mass maps*, *JCAP* **2024** (2024) 024 [[2307.11711](#)].
- [37] L.E. Bleem, B. Stalder, T. de Haan, K.A. Aird, S.W. Allen, D.E. Applegate et al., *Galaxy Clusters Discovered via the Sunyaev-Zel'dovich Effect in the 2500-Square-Degree SPT-SZ Survey*, *ApJS* **216** (2015) 27 [[1409.0850](#)].
- [38] E.J. Baxter, R. Keisler, S. Dodelson, K.A. Aird, S.W. Allen, M.L.N. Ashby et al., *A Measurement of Gravitational Lensing of the Cosmic Microwave Background by Galaxy Clusters Using Data from the South Pole Telescope*, *ApJ* **806** (2015) 247 [[1412.7521](#)].
- [39] ATACAMA COSMOLOGY TELESCOPE COLLABORATION collaboration, *Evidence of lensing of the cosmic microwave background by dark matter halos*, *Phys. Rev. Lett.* **114** (2015) 151302.
- [40] M.S. Madhavacheril, C. Sifón, N. Battaglia, S. Aiola, S. Amodeo, J.E. Austermann et al., *The Atacama Cosmology Telescope: Weighing Distant Clusters with the Most Ancient Light*, *ApJL* **903** (2020) L13 [[2009.07772](#)].
- [41] A. Huchet and J.-B. Melin, *A measurement of cluster masses using Planck and SPT-SZ CMB lensing*, *arXiv e-prints* (2024) arXiv:2402.18346 [[2402.18346](#)].

- [42] S. Raghunathan, F. Bianchini and C.L. Reichardt, *Imprints of gravitational lensing in the planck cosmic microwave background data at the location of wise \times SCOS galaxies*, *Phys. Rev. D* **98** (2018) 043506.
- [43] E.S. Rykoff, E. Rozo, M.T. Busha, C.E. Cunha, A. Finoguenov, A. Evrard et al., *redMaPPer. I. Algorithm and SDSS DR8 Catalog*, *ApJ* **785** (2014) 104 [1303.3562].
- [44] J.E. Geach and J.A. Peacock, *Cluster richness-mass calibration with cosmic microwave background lensing*, *Nature Astronomy* **1** (2017) 795 [1707.09369].
- [45] E.J. Baxter, S. Raghunathan, T.M. Crawford, P. Fosalba, Z. Hou, G.P. Holder et al., *A measurement of CMB cluster lensing with SPT and DES year 1 data*, *MNRAS* **476** (2018) 2674 [1708.01360].
- [46] The Dark Energy Survey Collaboration, *The Dark Energy Survey*, *ArXiv Astrophysics e-prints* (2005) [astro-ph/0510346].
- [47] T. McClintock, T.N. Varga, D. Gruen, E. Rozo, E.S. Rykoff, T. Shin et al., *Dark Energy Survey Year 1 results: weak lensing mass calibration of redMaPPer galaxy clusters*, *MNRAS* **482** (2019) 1352 [1805.00039].
- [48] S. Raghunathan, S. Patil, E. Baxter, B.A. Benson, L.E. Bleem, T.L. Chou et al., *Mass Calibration of Optically Selected DES Clusters Using a Measurement of CMB-cluster Lensing with SPTpol Data*, *ApJ* **872** (2019) 170 [1810.10998].
- [49] J.E. Austermann, K.A. Aird, J.A. Beall, D. Becker, A. Bender, B.A. Benson et al., *SPTpol: an instrument for CMB polarization measurements with the South Pole Telescope*, in *Millimeter, Submillimeter, and Far-Infrared Detectors and Instrumentation for Astronomy VI*, W.S. Holland and J. Zmuidzinas, eds., vol. 8452 of *Society of Photo-Optical Instrumentation Engineers (SPIE) Conference Series*, p. 84521E, Sept., 2012, DOI [1210.4970].
- [50] S. Raghunathan, S. Patil, E.J. Baxter, F. Bianchini, L.E. Bleem, T.M. Crawford et al., *Measuring galaxy cluster masses with CMB lensing using a Maximum Likelihood estimator: statistical and systematic error budgets for future experiments*, *JCAP* **2017** (2017) 030 [1705.00411].
- [51] M.S. Madhavacheril and J.C. Hill, *Mitigating foreground biases in CMB lensing reconstruction using cleaned gradients*, *PhRvD* **98** (2018) 023534 [1802.08230].
- [52] S. Raghunathan, G.P. Holder, J.G. Bartlett, S. Patil, C.L. Reichardt and N. Whitehorn, *An inpainting approach to tackle the kinematic and thermal SZ induced biases in CMB-cluster lensing estimators*, *JCAP* **2019** (2019) 037 [1904.13392].
- [53] J.E. Carlstrom, P.A.R. Ade, K.A. Aird, B.A. Benson, L.E. Bleem, S. Busetti et al., *The 10 Meter South Pole Telescope*, *PASP* **123** (2011) 568 [0907.4445].
- [54] J.A. Sobrin, A.J. Anderson, A.N. Bender, B.A. Benson, D. Dutcher, A. Foster et al., *The Design and Integrated Performance of SPT-3G*, *ApJS* **258** (2022) 42 [2106.11202].
- [55] D. Dutcher, L. Balkenhol, P.A.R. Ade, Z. Ahmed, E. Anderes, A.J. Anderson et al., *Measurements of the E-mode polarization and temperature-E-mode correlation of the CMB from SPT-3G 2018 data*, *PhRvD* **104** (2021) 022003 [2101.01684].
- [56] M.R. Calabretta and E.W. Greisen, *Representations of celestial coordinates in FITS*, *A&A* **395** (2002) 1077 [astro-ph/0207413].
- [57] B. Flaugher, H.T. Diehl, K. Honscheid, T.M.C. Abbott, O. Alvarez, R. Angstadt et al., *The Dark Energy Camera*, *AJ* **150** (2015) 150 [1504.02900].
- [58] I. Sevilla-Noarbe, K. Bechtol, M. Carrasco Kind, A. Carnero Rosell, M.R. Becker, A. Drlica-Wagner et al., *Dark Energy Survey Year 3 Results: Photometric Data Set for Cosmology*, *ApJS* **254** (2021) 24 [2011.03407].
- [59] E.S. Rykoff, E. Rozo, D. Hollowood, A. Bermeo-Hernandez, T. Jeltema, J. Mayers et al., *The RedMaPPer Galaxy Cluster Catalog From DES Science Verification Data*, *ApJS* **224** (2016) 1 [1601.00621].

- [60] K. Levy, S. Raghunathan and K. Basu, *A foreground-immune CMB-cluster lensing estimator*, *JCAP* **2023** (2023) 020 [2305.06326].
- [61] J.F. Navarro, C.S. Frenk and S.D.M. White, *The Structure of Cold Dark Matter Halos*, *ApJ* **462** (1996) 563 [astro-ph/9508025].
- [62] B. Diemer and M. Joyce, *An Accurate Physical Model for Halo Concentrations*, *ApJ* **871** (2019) 168 [1809.07326].
- [63] M. Oguri and M. Takada, *Combining cluster observables and stacked weak lensing to probe dark energy: Self-calibration of systematic uncertainties*, *PhRvD* **83** (2011) 023008 [1010.0744].
- [64] M. Oguri and T. Hamana, *Detailed cluster lensing profiles at large radii and the impact on cluster weak lensing studies*, *MNRAS* **414** (2011) 1851 [1101.0650].
- [65] Y. Omori, *Agora: Multi-Component Simulation for Cross-Survey Science*, *arXiv e-prints* (2022) arXiv:2212.07420 [2212.07420].
- [66] E.M. George, C.L. Reichardt, K.A. Aird, B.A. Benson, L.E. Bleem, J.E. Carlstrom et al., *A Measurement of Secondary Cosmic Microwave Background Anisotropies from the 2500 Square-degree SPT-SZ Survey*, *ApJ* **799** (2015) 177 [1408.3161].
- [67] A. Farahi, A.E. Evrard, E. Rozo, E.S. Rykoff and R.H. Wechsler, *Galaxy cluster mass estimation from stacked spectroscopic analysis*, *MNRAS* **460** (2016) 3900 [1601.05773].
- [68] T.M.C. Abbott, M. Aguena, A. Alarcon, S. Allam, S. Allen, J. Annis et al., *Dark Energy Survey Year 1 Results: Cosmological constraints from cluster abundances and weak lensing*, *PhRvD* **102** (2020) 023509 [2002.11124].
- [69] S. Grandis, J.J. Mohr, M. Costanzi, A. Saro, S. Bocquet, M. Klein et al., *Exploring the contamination of the DES-Y1 cluster sample with SPT-SZ selected clusters*, *MNRAS* **504** (2021) 1253 [2101.04984].
- [70] A. Zonca, L. Singer, D. Lenz, M. Reinecke, C. Rosset, E. Hivon et al., *healpy: equal area pixelization and spherical harmonics transforms for data on the sphere in python*, *Journal of Open Source Software* **4** (2019) 1298.
- [71] K.M. Górski, E. Hivon, A.J. Banday, B.D. Wandelt, F.K. Hansen, M. Reinecke et al., *HEALPix: A Framework for High-Resolution Discretization and Fast Analysis of Data Distributed on the Sphere*, *ApJ* **622** (2005) 759 [arXiv:astro-ph/0409513].
- [72] G. Van Rossum and F.L. Drake, *Python 3 Reference Manual*, CreateSpace, Scotts Valley, CA (2009).
- [73] P. Virtanen, R. Gommers, T.E. Oliphant, M. Haberland, T. Reddy, D. Cournapeau et al., *SciPy 1.0: Fundamental Algorithms for Scientific Computing in Python*, *Nature Methods* **17** (2020) 261.
- [74] S. van der Walt, S.C. Colbert and G. Varoquaux, *The NumPy Array: A Structure for Efficient Numerical Computation*, *Computing in Science and Engineering* **13** (2011) 22 [1102.1523].
- [75] A.M. Price-Whelan, B.M. Sipőcz, H.M. Günther, P.L. Lim, S.M. Crawford, S. Conseil et al., *The Astropy Project: Building an Open-science Project and Status of the v2.0 Core Package*, *AJ* **156** (2018) 123.
- [76] Wes McKinney, *Data Structures for Statistical Computing in Python*, in *Proceedings of the 9th Python in Science Conference*, Stéfan van der Walt and Jarrod Millman, eds., pp. 56 – 61, 2010, DOI.